THE ASTRONOMICAL JOURNAL, 116:972–980, 1998 August

THE PHOTOMETRIC GROWTH OF TWO SHOEMAKER-LEVY 9 IMPACT SITES ON JUPITER

CURTIS MANNING AND HYRON SPINRAD
Department of Astronomy, 601 Campbell Hall, University of California, Berkeley, Berkeley, CA 94720; cmanning@astro.berkeley.edu, hspinrad@astro.berkeley.edu

MICHAEL E. BROWN
Division of Geological and Planetary Sciences, Mail Stop 150-21, California Institute of Technology, Pasadena, CA 91125; mbrown@boondog.gps.caltech.edu

RAY L. NEWBURN
Jet Propulsion Laboratory, 4800 Oak Grove Drive, Pasadena, CA 91109; ray@scn5.jpl.nasa.gov

AND

DAVID SCHLEGEL
Department of Physics, University of Durham, South Road, Durham DH1 3LE, England, UK; djschlegel@durham.ac.uk
Received 1998 February 3; revised 1998 March 17

ABSTRACT

We present our findings on the photometric variability of the impact spots of comet Shoemaker-Levy 9 (SL 9) in the Jovian atmosphere. Extensive imaging and differential photometry of impact spots in the methane band (8950/90 Å) have enabled us to conservatively extract their photometric contribution from that of Jupiter. In this methane band, the SL 9 spots appear brighter than the surrounding Jovian surface because they lie above the main concentrations of methane that overlie the cloud tops. Our observations of two well-observed and isolated spots, H and Q1, indicate that spots experience a photometric growth that initially approximates a power law in time of index 0.3 and then appears to level off in the case of the H spot. We consider two explanations for the brightening of spots: (1) the dispersal of high optical depth core regions and (2) the coagulation of dust from the atomized or fragmented cometary ejecta. The former has been rejected because one spot, H, which was disrupted by a cyclonic storm, exhibited no discontinuity in its rate of photometric growth that would correspond to the disruption. We adopt the second as a working hypothesis because the growth of grains is consistent with our observations and has been cited as the cause for the observed changes in the integrated optical depth in the near-IR and the UV. We propose a simple model in which sites for grain nucleation are provided by the chemical interaction of cometary material and the shocked Jovian atmosphere and in which grain growth is restrained by the diminishing availability of raw materials for grain formation on timescales inversely proportional to the original aerosol density. This model, applied to a volumetric power-law distribution of aerosols, can produce an integrated scattering amplitude growth rate closely resembling our observations.

Key words: comets: individual (Shoemaker-Levy 9) — planets and satellites: individual (Jupiter)

1. INTRODUCTION

In July of 1994, the 20-odd components of Comet Shoemaker-Levy 9 fell into the southern hemisphere of Jupiter. These events were the focus of a large and diverse scientific effort to understand the nature of the impactors and their effect on Jupiter. At that time, the 40 inch (1 m) Nickel Telescope at Lick Observatory was used to gather as much optical imaging data as possible using three narrow-band filters centered on 4260, 5580, and 8950 Å, with a width of 90 Å. In this report, we emphasize images in the methane band, 8950 Å. In the two shorter wave filters, the impact spots appear dark because of the low albedo of cometary material. With the methane filter, however, they appear bright relative to the Jovian surface because of the screening provided by the high optical depth of methane overlying the cloud tops in the impacted area ($\sim 43°$ south latitude). Thus the ejecta seen in these images was deposited above the main concentrations of methane. A differential technique was devised to remove the contribution of the site-specific, static Jovian upper atmosphere from the images, yielding normalized, integrated photometric spot counts that are insensitive to the position of the spot on this disk. A careful analysis of the photometric evolution of impact spots may provide information on the formation and distribution of aerosols and dust grains in the upper atmosphere of Jupiter.

2. OBSERVATIONS AND INITIAL PROCESSING

The SL 9 impact sites were extensively imaged with a narrow methane filter, 8950/90 Å, on the 40 inch Nickel Telescope at Lick Observatory during the period 1994 July 16–August 6 UT. These images form the basis for our analysis of the photometric variability of impact spots. The telescope was fitted with an Orbit 2048^2 CCD camera (0.″37 pixel^{-1}), and integration times for night exposures were 14 s, resulting in a surface brightness of ~ 8000 ADU pixel^{-1}. The images were cleaned and flat-fielded using sky flats taken during the afternoon. They were subsequently rotated to horizontal and trimmed to a size slightly larger than the planet (121 pixels square).

At typical Lick seeing (FWHM $\sim 2''$), the images are oversampled. For most images, seeing varied from $\sim 1''$ to 3.″5. Over 2000 images of Jupiter in the methane band were taken during the period from July 16 to 29, although the days of July 21, 22, 25, and 26 UT were partly to completely cloudy. There was spotty coverage in early August as well,

but only one image from August 6 UT was used, because image quality was mediocre and by then many spots had dispersed to the point that it was difficult to determine their boundaries.

3. PHOTOMETRY OF IMPACT SITES

Our analysis of the spot brightness relies on carefully subtracting "prespot" Jovian images from "postspot" images. Thus the photometric parameters and results are differential, analogous to the differential photometry of stars in reflection nebulae. We feel this treatment removes the necessity for a deep physical understanding of the Jovian stratospheric layers. We now explain in detail our method of photometric reduction.

The images were taken under varying conditions, requiring careful control of variables to ensure high-quality subtractions. Because of the photometric irregularities of Jupiter in the impact zone, it was found to be necessary to select only images having matching System III longitudes to within $\sim 0\overset{\circ}{.}5$. While the requirement that longitudes of prespot and postspot images must match severely limits the number of useful images, we benefit by keeping the quality of our data high. In addition, although the phase angle changed very little over the course of the measurements, the Earth-Jupiter distance varied by ~ 0.2 AU during the first two weeks of observations, requiring the images to be resized to match a standard. The photometric normalization of the images also requires a standard image. Therefore, a "Jupiter average" was produced to serve as a standard both for the diameter and for total counts. This standard image is a carefully registered and co-added set of seven images from July 20. In order to create a photometrically smooth standard, extraneous large features such as the Great Red Spot (GRS) and superposed Jovian moons, with their high-methane filter brightness, were removed from all images and replaced with a featureless section of another image whose counts were normalized so that the addition appeared seamless. This standard, hereafter referred to as the "Jupiter average," was also used to normalize the counts of images containing impact spots.

In making the image pairs (see Figs. 1*a* and 1*b*) ready for subtraction, the north-south diameter of each is adjusted to match that of the Jupiter average, which requires the simultaneous matching of their point-spread functions (PSFs). We assume that the PSF is isotropic and diagnose it by the gradient of counts at the poles. The diameter normalization factors, applied to each *original* image, yield image pairs of equal diameter but with generally different PSFs. Thus, of the image pairs, the one with the best seeing must be convolved with a Gaussian to simulate the same seeing as the poorer image. Images that have been processed to the point of having all extraneous features (e.g., the GRS or moons) replaced with analogous sections of the Jupiter average, having their diameters normalized, and having compatible PSFs are hereafter called "sized image pairs." Following registration of the images, the prespot is subtracted from the postspot and the result is analyzed. Figure 2 displays central meridian and equatorial photometric profiles of a typical sized image pair. Please note that the abscissa of graphic images of subtractions are expressed in pixels rather than arcseconds, because the variation of Jupiter's distance during the period of observations makes it impossible to assign a physical scale to a pixel. In the case of subtractions, the appropriate physical scale is the apparent diameter of the planet referred to a standard—the Jupiter average, in this case.

To reach a target 5% photometric precision, pixel counts had to be normalized in a robust manner. While the counts of sized "prespot" images are easily normalized to the standard if no impact spots exist on the image, the presence of large impact spots can increase the total counts of images by up to $\sim 2\%$. Neglecting this factor during normalization will result in a depressed "continuum" value. The average surface brightness of the Jupiter average is ~ 8000 counts pixel^{-1}, while the average surface brightness of impact spots rarely exceeds 1% of this. As a result, a 1% error in the continuum will introduce a major uncertainty in the integrated spot counts, although the core of the spot will appear largely unaffected. Thus, before the normalization, spots and irregularities on the prespot image must be excised and replaced with analogous sections of the Jupiter average whose counts have been adjusted to produce a seamless boundary. The image is then normalized to the Jupiter average by requiring that the total counts in the image match that of the Jupiter average. The product of the normalization factor and the matrix of the sized prespot image (*with* the spots but without the irregularities) then represents the proper normalization. Please note for future reference that the contribution of these spots to the total can be estimated to first order by subtracting from the counts in each excised region the counts in each Jupiter-average patch used to replace them. This information will come in handy in normalizing the postspot image.

The postspot image is processed in a somewhat different way, because the effects of the impacts are often so widespread in later images that the above procedure is impractical. Let us initially assume that the *prespot* image has no impact spots of any kind on it. We normalize the postspot image to the standard as if there were *no* contribution from spots and, then, digitally subtract the counts of each pixel of the registered prespot image from the corresponding element of the postspot image. This image necessarily has total counts very near zero, although we expect there to be an excess in the impact zone and a net deficit in the remainder. We take the sum of the excess counts in the horizontal swath that includes all impact spots and divide by the total counts of the standard. This gives the first-order fractional contribution to the total counts from all spots on the postspot image. This is used to correct the original normalization and thus to produce a better approximation to impact-spot contributions in the swath. This process is applied iteratively until it converges.

When the prespot image has impact sites from other fragments it is important to add their contribution to the total counts of the swath in the postspot image, because the excess counts of the prespot image subtract from those of the postspot image, thus causing an underestimation of the spot contribution to photometric brightness in the swath used to correct the normalization. As mentioned above, during the normalization process of the prespot image, the counts contributed by impact spots in the prespot image are estimated by the difference in total counts of the area affected by the spots and that of the patches from the Jupiter average used to replace them. Figures 1*a* and 1*b* show an example of a prespot and postspot image pair taken from July 17 and 27.

The registration of prespot and postspot images is critical to a good subtraction. Since the images are oversampled,

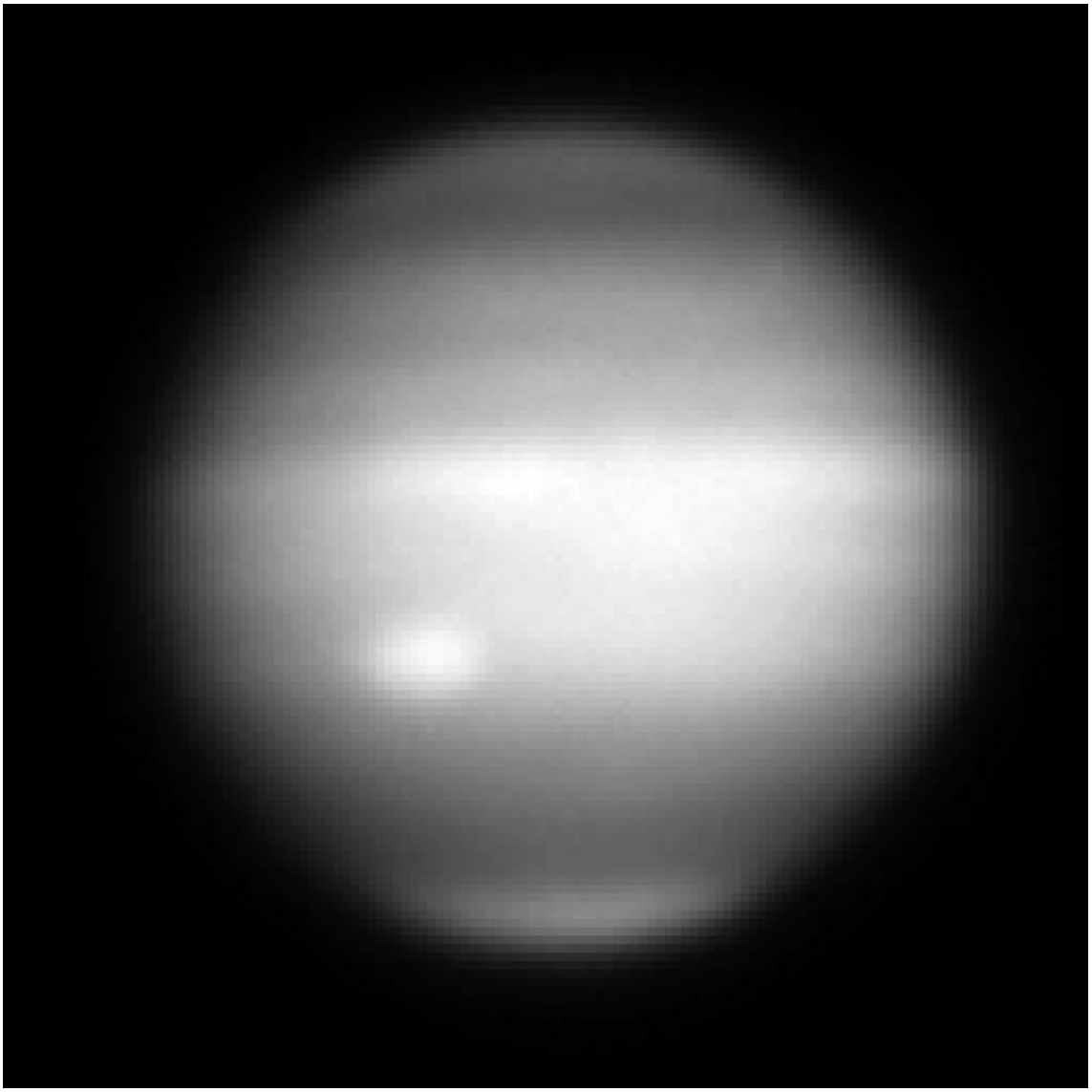

FIG. 1.—(*a*) Prespot image from July 17, with central meridian at 95°.886. The image is oriented with Jupiter's north pole up, the terminator on the left, and east to the right. (*b*) Corresponding postspot image from July 27, with central meridian at 96°.036. Once both images are properly sized and normalized (see text), the prespot is subtracted from the postspot. (*c*) In this image, a matrix element with zero counts is shown as a middle grey. The impact spots are, from left to right, E, H, Q1, and G. The rectangular region just below the equator is the replacement of the Great Red Spot from the Jupiter-average image; the dark band that appears in it is a common feature of the Jupiter-average images but is apparently disrupted near the GRS. The irregularities in the northern equatorial region are due to the lack of registration of large-scale features, resulting from Jupiter's differential rotation being summed over 10 days.

they may be conservatively shifted in any direction by using standard techniques of subpixel shifting. Shifts of less than ~ 0.1 pixels are seen to produce significant changes in the subtraction when the images are near optimal registration. Superposing "profile" averages of rows and columns of prespot and postspot images also helps as a diagnostic (see Fig. 2). Often at this level, one must go back and recheck the sizing and PSFs to remove obstinate edge effects. Once an optimal subtraction has been attained, it is easy to extract the total counts of a spot by specifying the boundary of its extent and summing the counts within. Images of the registered matrix subtractions of normalized prespot images from postspot images show the bright impact spots over an essentially homogeneous background (see Fig. 1*c*), save in the area of the northern equatorial bands, where the effects of differential rotation and its intrinsic photometric unevenness combine to produce large-scale photometric variations. The flatness of the resulting "continuum" in the impact zone (see, e.g., Fig. 3) gives us confidence in the resulting totals.

4. RESULTS

We sought prespot and postspot image pairs that could be combined to yield information on the variability of the integrated photometric brightness of spots in time and in terms of position on the Jovian disk. A subset of 16 image pairs were chosen for the final analysis. These pairs are listed in Table 1 below. Column (2) gives the prespot image designation, column (3) is the time measured in days from 1994 July 1, 0000 UT, and column (4) gives the System III central meridian longitude at the time the image was taken. The next three columns list the same data for the postspot. Column (8) tells which spots were measured from that image pair. Note that Q1 had not yet landed at the time of

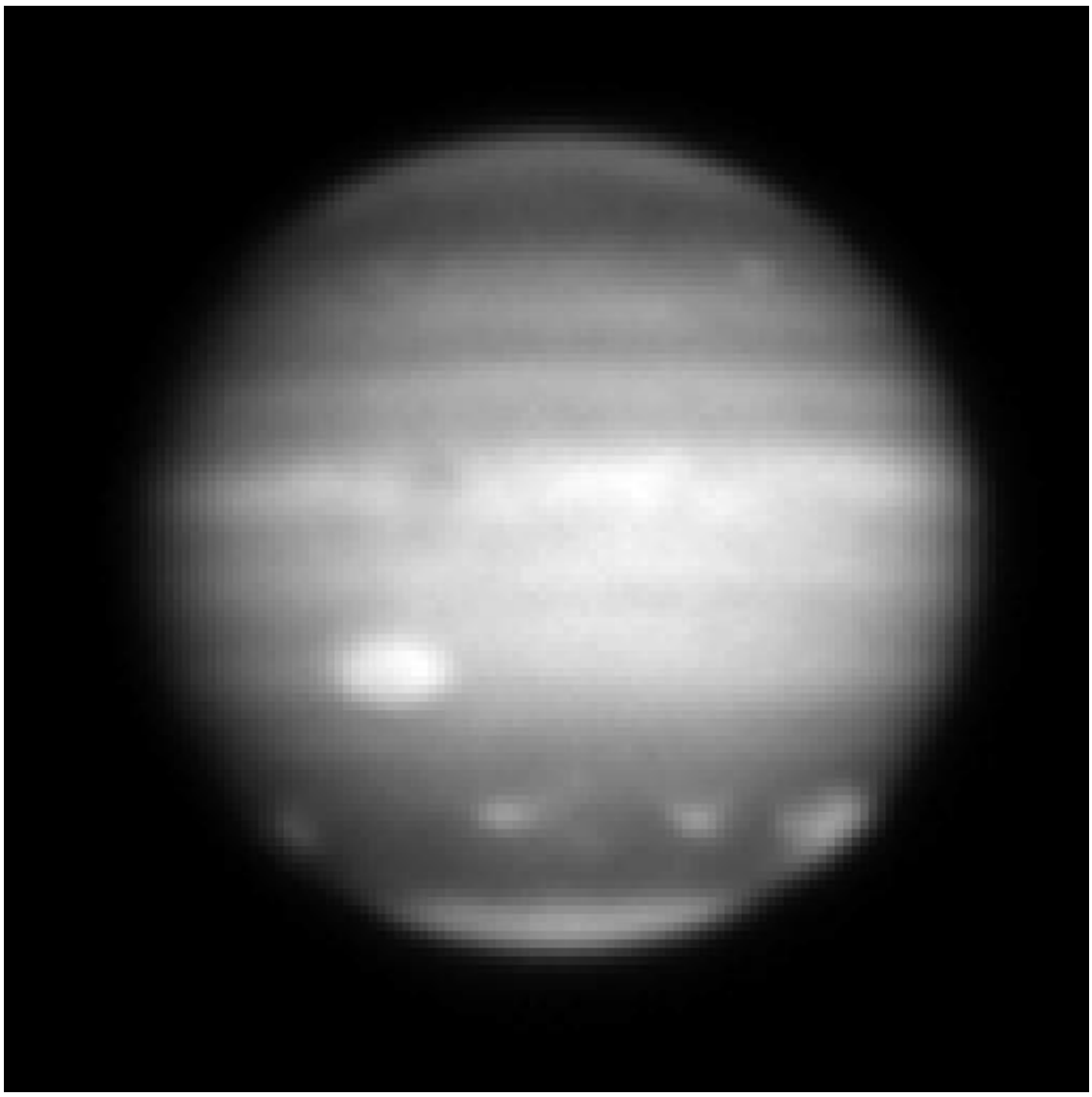

FIG. 1.—*Continued*

the first five postspot images. The longitude of the spot relative to the central meridian can be extracted by noting the true longitudes of the spots (63° [99°] for the Q1 [H] spots) and the central meridian value of the prespot and postspot images. In all cases, the relative longitudes are less than $\pm 45°$.

4.1. *Sources of Error*

Errors in the spot subtractions may enter through the inherent uncertainty in the proper value of the fitting parameters used to accomplish the subtractions. Analysis of error propagation shows that, of these, there are two main sources of error: uncertainty in the boundaries of the spot and the north-south registration of the images, both with uncertainty values usually in the range $\sim 1.8\%$–4%. Analysis of a number of the subtractions show that the total error averages $\sim 6.5\%$ per subtraction, with a mean variation of only about 0.4%. The two subtractions involving the image from August 6 (refer to the postspot on "37 July" in Table 1) required additional manipulation to produce a satisfactory fit because of problems with the flat-fielding of the postspot. Error propagation shows that the error per subtraction for this date is $\sim 7.6\%$. Additional error may arise from photometric irregularities on the surface of Jupiter, which may move into or out of the spot boundaries on timescales of a few days. This is due to the shear in the zonal winds, which approaches 10 m s^{-1} per degree of latitude. But the density of these irregularities is low, and they are not expected to introduce any significant additional error to the overall trends in the data.

4.2. *Integrated Spot Brightness as a Function of Position on the Jovian Disk*

In order to learn the possible variation of integrated photometric brightness of spots as a function of position on the disk, we require that on a given day there should be data over a wide range of relative longitude, where "relative longitude" is the difference between the longitudes of the central meridian and that of the spot. Good data exist on the L, H, and Q1 spots, but the results are hard to interpret: The L spot (as seen at 4+ and 9+ days after impact) shows a $\sim 30\%$ increase in counts as the spot moves from the central meridian to the east, while the H and Q1 spots (seen at 1+ and 8+ days for H and 6+ days after impact for Q1)

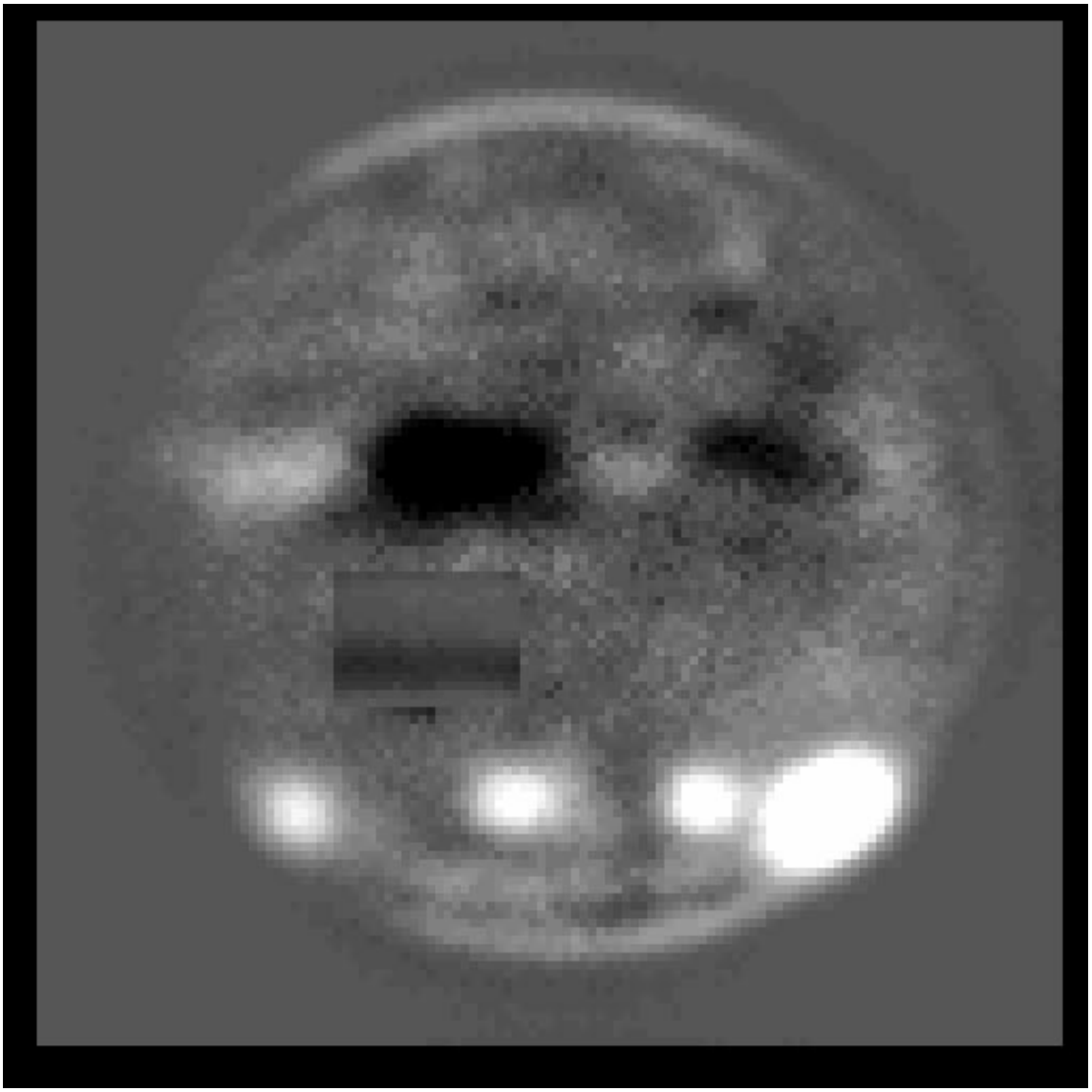

FIG. 1.—*Continued*

are consistent with the absence of dependence on angle. Attempts to explain the behavior of the L spot as a grain alignment effect have been unsuccessful. For the H and Q1 spots, those spots at relative longitudes whose absolute value is greater than arcsin 0.7 (i.e., about 45°) have integrated counts that are systematically lower than those produced at lower relative longitudes. This can be explained by the increased optical depth of methane for spot cores. That

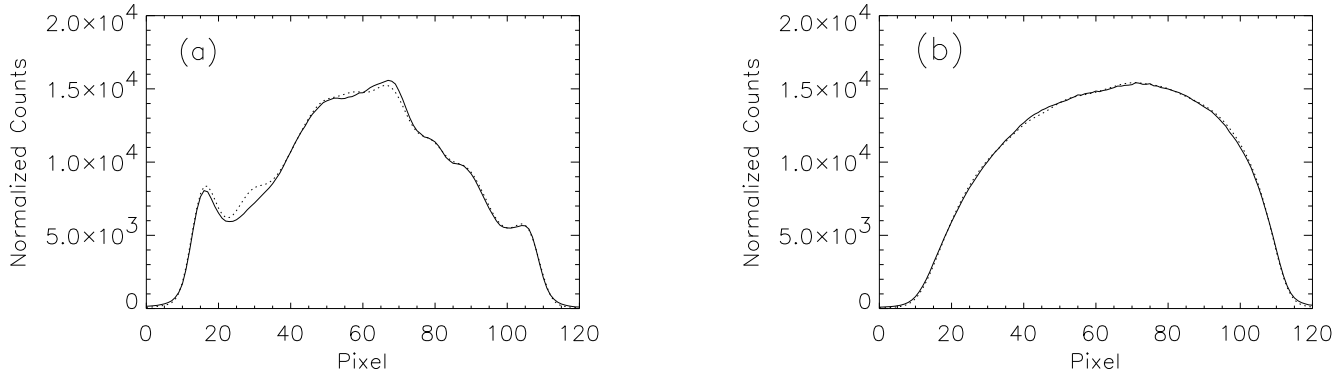

FIG. 2.—Surface brightnesses averaged over a 5 pixel (~1.″85) swath along (*a*) the central meridian and (*b*) the equator, once images (see Fig. 1) have been "sized," normalized, and registered. The prespot is the solid line. In this case, the postspot (*dotted line*) had to be convolved with a Gaussian to match the PSF of the prespot. The behavior at the edges guarantees that accurate sizing and PSF matching have been achieved. The asymmetry in (*b*) is due to the phase angle of ~10°, showing that the terminator is on the left.

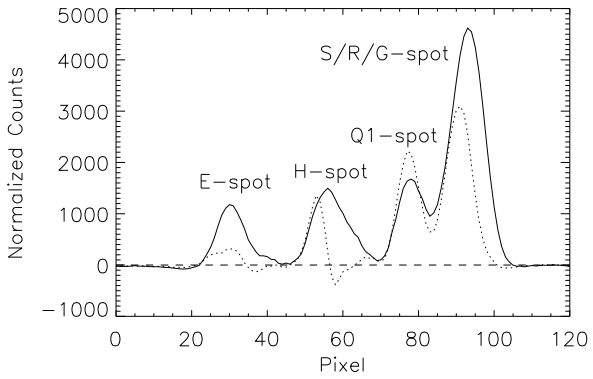

FIG. 3.—Average normalized counts over a 5 pixel swath centered approximately on latitude −43°. The solid line represents the subtraction of the July 17 image from the July 27 image (the same images used in Figs. 1*a* and 1*b*) and is designated the "27 − 17" plot. The dotted line is the subtraction of a July 20 prespot from the July 27 postspot (the "27 − 20" plot). Spot E landed by July 18, and H landed on July 19; the solid line represents the photometric brightness of spots E and H, and the dotted line represents the change in their brightness from the period of July 20–27. Both appear to have gained in brightness. The shift in position of spot H is caused by a passing anticyclone (see text). Spot Q1 landed late on July 20, so both plots should represent the same total counts. The higher peak of Q1 in the 27 − 20 plot is due to the fact that the seeing on July 20 was significantly better than that on July 17. The seeing on July 27 approached 1″. Since the G spot landed on July 18, it is subtracted off in the 27 − 20 plot, revealing the combined effects of the S and R spots.

it is insensitive to changes in relative longitudes up to $\approx 45°$ testifies to the fact that the bulk of the debris cloud lies above the main concentrations of methane and that the cloud is optically thin.

4.3. *Photometric Variability of Spots*

In order to learn the time evolution of the integrated photometric brightness of a given spot, we require that the spot be well isolated and that proper prespot and postspot image pairs exist for spots on a large number of days. The fact that Jupiter rotates ~ 2.42 times each Earth day and the

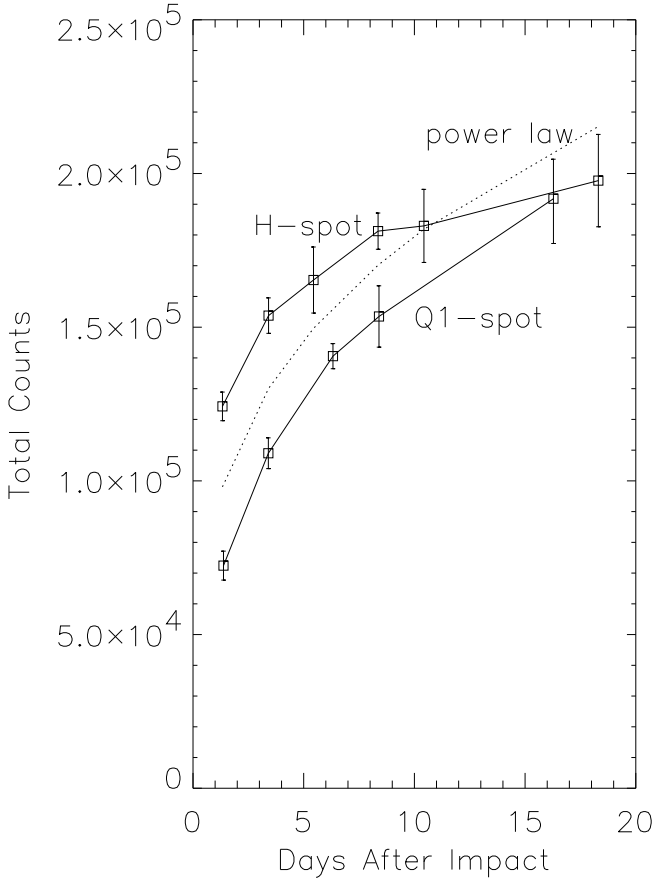

FIG. 4.—Growth in total photometric brightness normalized to the "Jupiter average" (see text) for spots H and Q1 in terms of days after impact. The dotted line is a $t^{0.3}$ power law with arbitrary normalization. The error bars at each point represent the result of 1 σ error propagation analysis. The error of a single subtraction is found to be $\sim 6.5\%$, but points that have multiple subtractions on a given day (see Table 1) have their error reduced by a factor of $N^{-1/2}$. The last point has an additional component of error because of problems with the initial flat-fielding of the postspot image, making the error $\sim 7.6\%$.

TABLE 1

PRESPOT AND POSTSPOT IMAGE PAIRS FOR SPOTS H AND Q1

	PRESPOT			POSTSPOT			
PAIR (1)	Image Number (2)	Date (3)	Central Meridian Longitude (4)	Image Number (5)	Date (6)	Central Meridian Longitude (7)	SPOT[a] (8)
1.....	17+d2436	17.233	62.578	20+d5250	20.128	62.606	H
2.....	17+d2467	17.252	79.032	20+d5291	20.146	78.366	H
3.....	17+d2513	17.274	97.922	20+d5324	20.169	98.211	H
4.....	17+d2480	17.258	84.429	22+d7002	22.220	84.464	H, Q1[a]
5.....	17+d2507	17.271	95.485	22+d7026	22.234	95.782	H
6.....	17+d2497	17.266	91.307	22+d7017	22.229	91.428	H
7.....	17+d2384	17.205	38.378	24+d9422	24.235	38.333	Q1
8.....	17+d2425	17.228	58.226	24+d9462	24.258	57.746	H, Q1
9.....	17+d2381	17.204	37.159	27+d1288	27.129	37.228	Q1
10.....	17+d2422	17.226	56.659	27+d1172	27.151	56.467	H, Q1
11.....	17+d2440	17.236	65.277	27+d1193	27.161	65.347	H, Q1
12.....	17+d2482	17.259	85.213	27+d1225	27.184	85.369	H, Q1
13.....	17+d2514	17.275	98.706	27+d1249	27.199	98.688	H, Q1
14.....	17+d2467	17.252	79.032	29+d3450	29.244	78.732	H, Q1
15.....	17+d2513	17.274	98.271	37+d4133	37.124	98.148	H, Q1
16.....	20+d5324	20.169	98.211	37+d4133	37.124	98.148	Q1

NOTE.—Cols. (2) and (5) present image numbers; cols. (3) and (6) give the time the image was taken, expressed as days elapsed from July 1 at 0000 UT; and cols. (4) and (7) give the System III central meridian longitude in degrees at that time.

[a] The time $t_{\rm impact} = 18.81$ (20.84) days at 99° (63°) longitude for spot H (Q1).

chance effect that Jupiter was only optimally observable for a maximum of ~3 hr per night result in image pairs almost invariably being spaced at least 2 days apart. The data on the H and the Q1 spots are ideal for these purposes. Figure 4 shows the extracted total counts of the H and Q1 spots as a function of the time elapsed since the impact. Because counts for H and Q1 were not seen to vary significantly for relative longitudes less than $\pm 45°$, days with data from more than one subtraction were averaged; thus, their individual errors can be combined in quadrature, leading to high confidence in some points. In each case, the resulting formal error was commensurate with the spread in extracted values for days with multiple subtractions. Reference to Table 1 will show the level of redundancy of image pairs on a given day.

The data for the first 10 days are thought to be excellent. We have eliminated spots whose longitude relative to the central meridian has an absolute value greater than arcsin 0.7, because uncertainties rise near the edge. Our results show (see Fig. 4) that the integrated brightness of these spots grew approximately in concert with a power law of index 0.3 during the first 10 days following the impacts (*dotted line*). We observe a normalized brightening of ~67%–100% for the H and Q1 spots, respectively, during this interval. Beyond the first 10 days, the quality and quantity of the data decline, but it is clear that the Q1 spot continues to photometrically brighten while the H spot appears to noticeably deviate from its earlier rate of increase. In view of the large settling timescale for dust grains (see § 5), the apparent leveling off in counts after 10 days may best be understood, in the case of the H spot, as the result of the dispersal of high-altitude dust, due to stratospheric winds, and zonal wind shear.

5. DISCUSSION

We have observed an increase in photometric spot counts, followed by an apparent leveling off in the case of the H spot, while spot Q1 appears to continue to rise. The cessation in the increase in counts of the H spot cannot be explained as being due to the settling of grains in the atmosphere, because the sedimentation time for dust of median radius ~0.5 μm is on the order of a month at 10 mbar (West et al. 1995). Estimates of mean dust radii are in the range of 0.20 μm (e.g., West et al. 1995; Muñoz, Moreno, & Molina 1996) and would imply an even longer timescale for sedimentation. The decline may be more plausibly understood as a dispersal of high-altitude dust grains by stratospheric winds, as has been noted of the L spot (Hammel et al. 1995). Our images of spot H show that, after about 4 days, much of the diffuse dust of the plume became spread into two spatial projections, one to the southeast and the other to the northeast. This was apparently caused by its interaction with an anticyclone passing in an easterly direction immediately to the north of the spot (Beebe 1996). Subtractions of pairs of postspot images from this period (see Fig. 3) show a net loss of counts in time to the southeast of the spot center and a gain to the northwest. This implies that the deep core of the spot was dragged by the interaction with the storm and was thus subjected to shear forces that could easily have disrupted the dense central core of the spot, as well as accelerating the dispersal of the high-altitude plume. The significant reduction in the rate of increase of total H counts noted in August can thus be largely attributed to the fact that H had been strongly disrupted. Spot Q1, which was not disrupted, retained much of its compact, symmetric shape and shows no sign of a departure from the power-law growth.

We have shown that the brightening of selected spots can be well represented as a power-law function of time with an index of ~0.3 in the first 10 days following the impact (see Fig. 4). The increase in the integrated photometric spot counts with time may be explained by either the dispersal of the high optical depth core regions or the physical growth of grains through the sweeping up of atomized or fragmented cometary material. If the increase in integrated spot counts was caused exclusively or substantially by the dispersal of the high optical depth core regions of the spots, then we should expect that a spot whose core was strongly disrupted by a passing storm would produce a discontinuity in the photometric growth rate at a time coinciding with the event. *Hubble Space Telescope* images of the H spot (Beebe 1996) show that the disruption began early on the third day following the impact. Note, however (Fig. 4), that integrated counts were not affected in a way that would support the hypothesis (see images in Beebe 1996). We therefore reject the former explanation.

With regard to the latter, relatively little is known about grain growth in the postimpact Jovian atmosphere. It is thought that some grain growth commenced shortly after the impact, while the plume was still expanding away from the atmosphere of Jupiter (Friedson 1998). In addition, West et al. (1995) noted that the optical depth of dust at 8930 Å, integrated over the surface that includes all spot ejecta, increased during the period July 23–August 24 from 1.1 to 1.5. Most of the increase was achieved by July 30 and was attributed to an increase in the mean radii of dust particles from 0.21 to 0.28 μm. Our observations, which began less than 1.5 days after the impacts, show a significant increase in brightening, although our observations encompass a smaller but earlier time interval. Since there exists evidence supporting the grain growth hypothesis, we adopt the latter as a working hypothesis.

6. A GRAIN GROWTH MODEL

It is possible to set the relative timescales for grain nucleation and growth if one knows the temperatures and relative concentrations of refractory elements, assuming there are no potential or stoichiometric barriers to overcome (Spitzer 1978). The range of concentrations of essentially cooled ejecta at various altitudes within the impact sites (see, e.g., Griffith et al. 1997) lead us to expect that the photometric growth of the diffuse ejecta blanket would be slower than that of the central core where the density of dust is much higher. Studies of the K and L sites (Bézard, Griffith, & Kelly 1997) less than a day after their impacts showed that at pressures of ~0.1 mbar, temperatures were elevated less than 30 K over the normal (which is typically between 100 and 150 K) and less at higher pressures. Since temperatures quickly returned to near normal following the plume impact and since the condensation temperatures of the principal grain-forming species is typically in excess of 1000 K (Spitzer 1978), we expect that the variation in temperatures within the various parcels will have a negligible effect on grain growth rates and therefore choose to ignore it.

Griffith et al. (1997) show that the actual quantities of Jovian gas entrained in the ballistic plume of the K impact appears to have been up to 1000 times that of the cometary

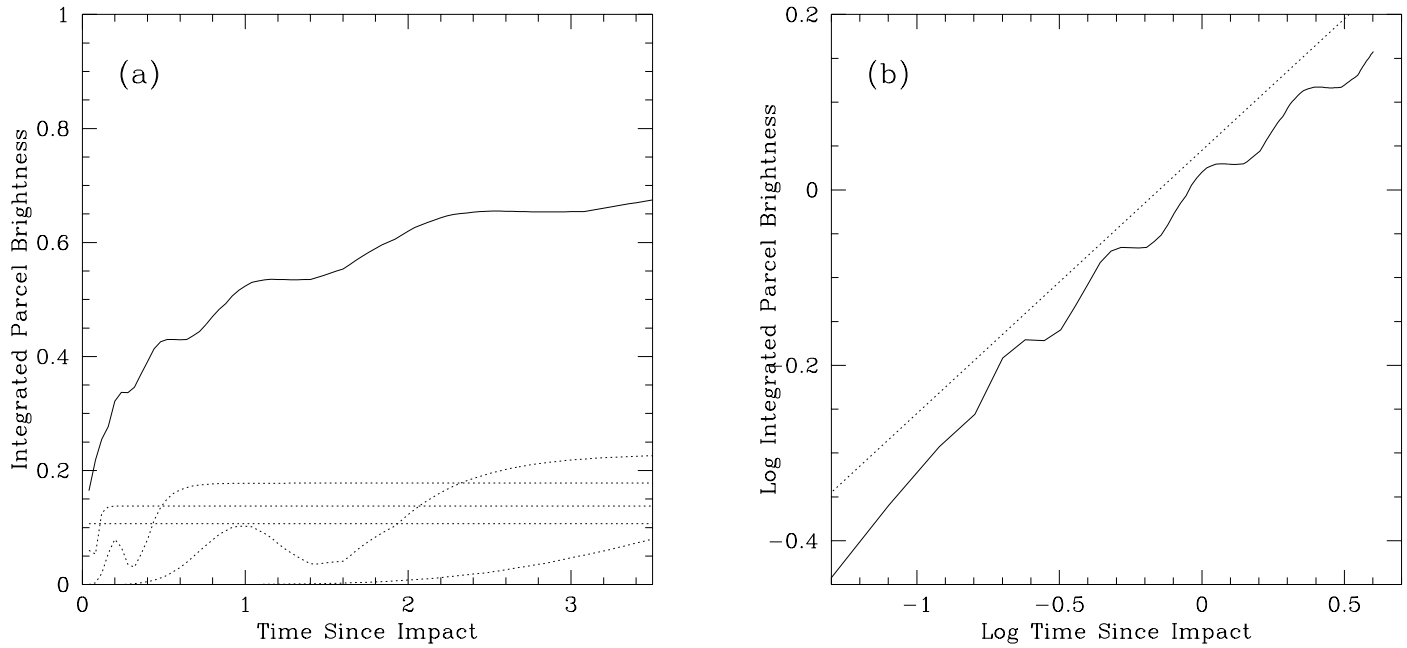

FIG. 5.—Grain model. (*a*) The scattering amplitude $B(t)$ (arbitrary normalization) output from a Mie code (Wiscombe 1997) applied to a refractory cloud represented by the distribution function, $\delta V \propto \rho^m \, \delta\rho$, with an index of $m = -2.16$, based on a simple grain growth model (see text). The density range of the cloud is 2500–1 and is divided into 10 equal parcels in log ρ. The solid line shows the sum of all 10 components, while the dotted lines represent the odd-numbered parcels, each multiplied by a factor of 2, so that the five might be seen as an approximation to the components of the total. The high-density parcels achieve their maximum early, but it is clear that low-density parcels have a greater total mass of grain-forming material. (*b*) Comparison of the growth of brightness (*solid line*) with a power law of slope 0.3 (*dotted line*).

material and that, according to the proximity to the fireball, material was heated, chemically altered, and thrown to distances approaching that of the widest extent of the cometary debris. The source for the majority of nuclei for condensation may thus plausibly be supposed to have been the Jovian gases—methane and ammonia—swept into the plume and dehydrogenated by the high temperatures of the impact (R. Saykally 1997, private communication), perhaps forming the seed nuclei of carbon and SiC within carbon-rich parcels and forming silicates and Al_2O_3 in oxygen-rich parts of the plume (Friedson 1998).

In compounding our grain growth model, our basic assumption is that the ejecta blanket can be characterized as the superposition of parcels of a range of densities, occupying volumes of varying size. We will characterize this with a general distribution function. We also assume that within each parcel, grain growth can be considered to be uniform and intercomparable through the parameters controlling grain growth. Below, we derive the equations of grain growth that will make this comparison possible.

In conformity with the considerations above, we assume a high density of nucleation sites, and we assume that the local ratio of the number density of nucleation sites, n_n, to the total material density, ρ_T, of fragmented and atomized cometary debris in the parcel is constant throughout the cloud. For a parcel characterized by a single refractory density, this density is composed of grains and their atomic grain precursors. Thus, we write

$$\rho_T = (4/3)\pi n_n \rho_{\rm gr} a^3 + n_a m_a \,, \tag{1}$$

where spherical grains of radius $a(t)$ are assumed, $\rho_{\rm gr}$ is the mass density of the grain itself, m_a is the mass of the (assumed) atomic grain precursors, and $n_a(t)$ is their number density. Assuming uniform growth, the maximum grain radius is

$$a_{\rm max} = \left(\frac{3\rho_T}{4\pi\rho_{\rm gr} n_n}\right)^{1/3} . \tag{2}$$

The rate of growth of the mass of a grain is $\dot{m}_{\rm gr}(t) = ka(t)^2 m_a n_a$, where k is a constant containing terms for the velocity of atoms and the sticking probability, both assumed uniform throughout the cloud. Grain growth may also be expressed as $\dot{m}_{\rm gr} = 4\pi\rho_{\rm gr} a^2 \dot{a}$, where $\dot{a}(t)$ is the derivative with respect to time. We solve these equations for $\dot{a}$ with the aid of equation (1):

$$\dot{a} = \frac{k}{4\pi\rho_{\rm gr}}\left(\rho_T - \frac{4\pi}{3}\,\rho_{\rm gr} n_n a^3\right). \tag{3}$$

Using equation (2), this becomes

$$\dot{a} = \tfrac{1}{3} k n_n (a_{\rm max}^3 - a^3) \,. \tag{4}$$

Note that when $a(t) \ll a_{\rm max}$ da/dt is constant, but that $a(t)$ declines exponentially as $a(t)$ approaches $a_{\rm max}$.

Solving for dt and integrating, equation (4) yields

$$t = \frac{3}{k n_n a_{\rm max}^2} \int_0^t \frac{dx}{1 - x^3} \,, \tag{5}$$

where $x = a(t)/a_{\rm max}$. We perform the integral and find that the time it takes to achieve a grain size of $a(t) = a_{\rm max}\, x$ is

$$t \propto \frac{1}{\rho_T}\left\{\ln\left[\frac{(1-x)^3}{1-x^3}\right] + 3\sqrt{3}\left[\arctan\left(\frac{2x+1}{\sqrt{3}}\right) - \arctan\left(\frac{1}{\sqrt{3}}\right)\right]\right\}, \tag{6}$$

where we have used the assumption that n_n and ρ_T observe a constant ratio within the cloud.

This function can be inverted so that time becomes the independent variable, enabling us to calculate the size parameter of grains as a function of time and the parcel density ρ_T. Grains in cloud parcels with large densities achieve radii comparable to $a_{\max}$ very quickly, while low-density parcels take much longer. The observed impact spots are viewed as a superposition of many densities.

As an initial, minimal modeling assumption, we assume that the volume occupied by impact residue in the density range $\rho \pm \delta\rho/2$ is δV, where the subscript in ρ_T has been dropped. It is hypothesized that the "filling factor" δV is a power law of the density: $\delta V(\rho) \propto \rho^m \delta\rho$, where m is a tunable constant. The mass of this "parcel" is $\delta M(\rho) = \rho \delta V(\rho)$. We suppose that the cloud has a density range of $\rho_{\max} = 2500$ to $\rho_{\min} = 1$ (arbitrary units) and divide that range into 10 equal parts in log ρ, evaluating the density at the median point of each bin. This is acceptable because it turns out that the best fit to the data shows that the mass in parcels of density per unit $\delta\rho$ is only a weak function of ρ (see contributions of individual parcels in Fig. 5). In order to predict the photometric brightening that would accompany grain growth, one must use Mie theory, which applies to spherical dielectric grains; for a maximum grain radius of 0.28 μm (West et al. 1995), the size parameter in this methane band is $\sim$2.0, and scattering amplitudes are highly variable for sizes smaller than this. We acquired a Mie code (Wiscombe 1980) and, using the index of refraction $1.45 - 0.008i$ derived by West et al. (1995), applied it to the time-varying mean radii predicted by our cloud model. In running this code for the scattering angle of 170°, we found that the scattering amplitude is not sensitive to the imaginary part of the index of refraction when the real part is $\sim$1.45. When the real part is below 1.40, scattering amplitudes fall rather precipitously. The products of the scattering amplitudes, the volumes, and the densities for each parcel as a function of time are summed to produce the predicted integrated photometric brightness of spots as a function of time, $B(t)$.

Our goal is to reproduce the observed brightening rate, characterized by the power law displayed in Figure 4. The index of the distribution function, m, is used to tune the output, $B(t)$. The logarithm of $B(t)$ is then plotted against log t to determine the slope. In Figure 5*a*, we present the predicted photometric brightening of the 10-parcel cloud with a power-law index $m = -2.16$, together with the contributions from odd-numbered parcels (multiplied by a factor of 2), and in Figure 5*b* we present log $B(t)$ versus log t together with a line of slope 0.3 (with arbitrary normalization). It is apparent that the fit is satisfactory.

It is possible to interpret these results in two different ways: If this distribution function is deemed consistent with the actual distribution in the impact sites, then these results could be interpreted as supporting our simplified model of grain growth. On the other hand, given the assumed grain growth model, the slope m, which is required to produce a match with observations, provides information about the distribution function of impact parcels.

7. CONCLUSIONS

Using matching sets of "prespot" and "postspot" images, we have conservatively extracted the normalized integrated counts of spots H and Q1 to a high precision. Our results show that both the H and Q1 spots brighten at a rate approximated by a power law of index 0.3 for a period approaching 10 days following the impact. The principal cause of this effect is unlikely to be the dispersal of high column density material, but it is consistent with actual grain growth. We have modeled this growth by supposing that many nucleation sites are provided by chemical interaction of cometary material and the Jovian atmosphere in the hot plume during both its ejection and its reentry. One may convolve this simple grain-forming model with a distribution function of discrete parcels of density given by $\delta V(\rho) = \rho^m \delta\rho$, where ρ is the density, V is volume, and $m \sim -2.16$. Assuming homogeneous spherical grains, a Mie code was used to transform this distribution into a predicted rate of growth in brightness (see Fig. 5) that closely matches that of our observations (Fig. 4) during the first 10 days following the impacts.

In addition to the information currently presented, we also have extensive flat-fielded images of the C, A, and E spots; however, because high-quality prespot images do not exist for these spots, it is not possible to extract normalized counts, although growth may be measured through differencing pairs of postspot images. In addition, we have extensive imaging of the impactor complex, G/R/S, in all stages of its development, and this could be used for assessing the relative masses of these impactors.

We acknowledge the support of Remington Stone and the Mount Hamilton staff in the observation stage, and NASA grant 1-443833 and NSF grant AST 93-22119 in support of the analysis. Thanks to J. Melbourne for help in the reduction and to A. Bunker, D. Stern, C. Matzner, R. A. West, W. Wiscombe, and R. Saykally for helpful discussions during the compilation of this report.

REFERENCES

Beebe, R. F. 1996, in IAU Colloq. 156, The Collision of Comet Shoemaker-Levy 9 and Jupiter, ed. K. S. Noll, H. A. Weaver, & P. D. Feldman (Cambridge: Cambridge Univ. Press), 307
Bézard, B., Griffith, C. A., & Kelly, D. M. 1997, Icarus, 125, 331
Friedson, A. J. 1998, Icarus, 131, 179
Griffith, G. A., Bézard, B., Greathouse, T. K., Kelly, D. M., Lacy, J. H., & Noll, K. S. 1997, Icarus, 128, 275
Hammel, H. B., et al. 1995, Science, 267, 1288
Muñoz, O., Moreno, F., & Molina, A. 1996, Icarus, 121, 305
Spitzer, L. 1978, Physical Processes in the Interstellar Medium (New York: Wiley), 206
West, R. A., Karkoschka, E., Friedson, A. J., Seymour, M., Baines, K. H., & Hammel, H. B. 1995, Science, 267, 1296
Wiscombe, W. J. 1980, Appl. Opt., 19, 1509. (http://emlib.jpl.nasa.gov).